Effects of SMAT at cryogenic and room temperatures on the kink band and martensite formations with associated fatigue resistance in a β-metastable titanium alloy

Pierre Maurel, Laurent Weiss, Philippe Bocher, Thierry Grosdidier

Version of Record: https://www.sciencedirect.com/science/article/pii/S0921509320316816
Manuscript_0f3d6f3775e08f605d0920821356096d

Effects of SMAT at cryogenic and room temperatures on the kink band and martensite formations with associated fatigue resistance in a β-metastable titanium alloy

Pierre Maurel[a,b,c,*], Laurent Weiss[a], Philippe Bocher[b,**], Thierry Grosdidier[a,c,**]

[a] *Université de Lorraine, Laboratoire LEM 3, UMR CNRS 7239, 7 Rue Félix Savart, 57073 Metz, France*
[b] *Laboratoire d'Optimisation des Procédés de Fabrication Avancés (LOPFA), École de Technologie Supérieure, 1100 rue Notre-Dame Ouest, Montréal, Canada*
[c] *LABoratoire d'EXcellence "Design of Alloy Metals for low-mAss Structures" (LABEX-DAMAS), 7 rue Félix Savart, 57073 Metz, France*

Abstract

Surface Mechanical Attrition Treatment (SMAT) has been carried out at cryogenic and room temperatures on a 5553 β-metastable Ti alloy to describe its effects on the modification of the microstructure and fatigue properties. The cryogenic temperature promoted the martensitic transformation and the width of the kink bands produced by SMAT. The kink bands formation was promoted by the high strain rates of the SMAT process. The samples SMATed at cryogenic temperature showed an increase in fatigue resistance, by about 8%, compared to samples processed by SMAT at room temperature. This improvement was possibly due to a combination of several factors: compressive residual stresses, lower roughness, deeper formation of martensite and larger kink bands. On the contrary, the SMAT at room temperature did not provide any improvement in terms of fatigue compared to the polished condition. The large grain size provoked the appearance of subsurface crystallographic defects on which primary cracks initiated. This greatly limited the effectiveness of the reinforced surface layer produced by SMAT.

Keywords: Severe Plastic Deformation (SPD), Beta Titanium alloy, High Cycle Fatigue, Surface Mechanical Attrition Treatment (SMAT), Kink band, Cryogenic treatment

*Corresponding author.
**Secondary corresponding authors.
Email addresses: pierre.maurel@univ-lorraine.fr (Pierre Maurel), philippe.bocher@etsmtl.ca

Highlights

- Kink bands generated by the high strain rates induced by SMAT
- A lower kink band density in the first μm of SMATed surfaces
- Deeper martensitic formation and lower roughness for cryogenic SMAT
- Increased fatigue resistance for SMAT at cryogenic temperature

1. Introduction

The development of Severe Plastic Deformation (SPD) allowed the processing of materials with highly enhanced properties. Several reviews of the different processes highlighted the links between the microstructure refinement, high dislocation densities and significant increases of the strength and hardness [1–3]. Unfortunately, the resulting ductility drop is the main drawback of those property improvements. Most SPD techniques need immense loads on small sized samples with basic geometries, such as the High-Pressure Torsion [4] or the Equal Channel Angular Pressure [5]. This remains a significant limitation for up-scaling those processes to industrial applications.

As the external surface is usually the most demanding location in industrial parts due to high loads, corrosion, or friction, surface SPD processes were developed to promote the surface resistances in some applications. To this end, examples such as Burnishing [6], Laser Shock Peening [7], Ultrasonic Shot Peening (USP or USSP) [8] or Surface Mechanical Attrition Treatment (SMAT) [9–13] were developed. SMAT and USSP processes deform the surface by propelling a media on it (mainly metallic balls) and were developed from pre-strain shot-peening [10, 12, 14]. A long enough treatment also produces a significant grain refinement and surface property gradients. These surface SPD processes are well known for modifying wear resistance [15, 16], corrosion resistance [17, 18] and for introducing important compressive residual stresses. These high compressive residual stresses and finer

(Philippe Bocher), thierry.grosdidier@univ-lorraine.fr (Thierry Grosdidier)

microstructures at the surface are known to retard fatigue crack propagation and thus increase the fatigue resistance in aluminium alloys [14]. However, the roughness induced by surface nanostructuring may negatively impact the fatigue resistance, as shown on superalloys, stainless steels and aluminium [13, 19, 20].

In metastable austenitic stainless steels, in which the stress-assisted or strain-induced martensitic transformations could be triggered, performing SMAT at cryogenic temperature could be used to increase the fraction of hardening martensite towards higher depth as well as to modify the interplay between slip activity and martensite / twining formation [21, 22]. The deformation gradient formed by the surface modification generally produces gradients of different natures such as grain size, hardness, martensitic [22] and/or twinning [23] fractions. If the material is harder to deform at cryogenic temperatures, a significant decrease of the apparent surface roughness can be obtained [22]. Thus, an appropriate selection of processing parameters allowed to tailor the surface towards a broad range of hardness and roughness values [22].

The β-metastable Ti alloys are prone to the formation of stress assisted or strain induced martensites as well as mechanical twinning which can both compete with conventional plasticity mediated by dislocations. The occurrence of these deformation mechanisms depends on the stability of the β phase which, itself, is affected by its chemical composition [24, 25], the size of the β grains [26, 27], as well as the possible presence of a secondary phase [28, 29]. These mechanisms can be activated in various Ti alloys thereby exhibiting shape memory effect [30, 31], superelasticity [31–36] or strain-hardening behavior [3, 4, 37, 38] and affecting their tensile properties [28, 39, 40]. Superelasticity, due to the formation of stress-assisted martensite, significantly improves the low-cycle fatigue behavior in these alloys due to the reversible phase transformation which suppressed microplastic deformations [35]. The high-cycle fatigue domain would be less sensitive to this mechanism as the lower stress involved may not trigger the phase transformation. Also, the martensitic transformation may enhance the grain refinement obtained by severe plastic deformation [41]; this in turns may improve the high-cycle fatigue behavior. In β-metastable titanium alloys with a complete β microstructure, few studies revealed the possibility to activate a different deformation mech-

anism such as the formation of kink bands [42–47]. Although common to materials with high anisotropy [48, 49], kink bands rarely appear in body-centered cubic structures. Zheng et al. described in detail the formation of those deformation bands [43]. They are due to the accumulation of edge dislocations resulting in bands with random misorientations ranging mostly between 10° and 25° compared to the initial orientation. Three kink slip systems may be activated: $(112)[11\bar{1}], (123)[11\bar{1}], (101)[1\bar{1}\bar{1}]$. They induce a rotation of the crystal around three rotation axes, also called Taylor axes: $[1\bar{1}0], [5\bar{4}1], [12\bar{1}]$, respectively. As the kink bands are relatively thin, this mechanism effectively refines the microstructure by the introduction of a high density of high-angle boundaries. It has been confirmed that this deformation mechanism depends on the alloy composition ; as Sadeghpour et al. used the same deformation process on four different β-metastable titanium alloys and obtained kink bands in only one of these alloys [50]. Surprisingly, for Sadeghpour et al., one of the alloys that did not produce any kink band was the 5553 while Qin et al. showed the possibility to form kink bands in this 5553 alloy [45].

According to the previously described information, three main goals were set for this paper. First, exploring the possibility to trigger or not kink band formation using the SMAT process in the β-metastable 5553 titanium alloy. Indeed, kink bands were triggered in this same alloy by Split-Hopkinson bars [45] but not by shear punching [51]. Second, comparing the surface effects of SMAT at room and at cryogenic temperatures in terms of material properties and especially crystallographic transformations (martensitic and/or kink formations). Finally, discriminating any possible impact on fatigue resistance of the SMAT process.

2. Experimental Procedures

2.1. Material and surface treatments

The 5553 β-metastable titanium alloy studied in this paper was provided by Timet Savoie (France) as a slice of a forged billet. Its chemical composition was [wt%]: Mo 4.84, V 4.93, Al 5.29, Cr 3.04, Fe 0.3, O 0.14, C 0.008, N 0.004, Ti (balance). The alloy was solution-treated

at 925°C for 1 h in a vacuum furnace and water-quenched. This treatment allowed the alloy to retain a complete beta microstructure with an average grain size of about 260 μm.

Fig. 1 gives a sketch of the Surface Mechanical Attrition Treatment (SMAT) device used to treat the R. R. Moore fatigue samples (red) [52]. Two millimeters in diameter AISI 52100 steel shots were confined within the treatment chamber (green) and moved using an ultrasonic device (blue) vibrating at a frequency of 20 kHz with a 60 μm amplitude. When the vibrating device (sonotrode developed by SONATS [53]) was unused, the shots covered roughly 20% of the vibrating surface. The central section surface of the fatigue samples was set at a distance of 20 mm from the sonotrode. The SMAT duration for the treatment of the cylindrical samples was set to 40 min while the samples were rotating at a constant speed of 20 rpm. Copper heat sinks (in orange in Fig. 1) partly immersed in liquid nitrogen were fixed on both sample heads to maintain the samples at cryogenic temperature during the cryogenic treatments.

Three treatment conditions were studied and provided the following samples:

- Polished samples (P): these samples were machined to the dimensions, then heat-treated and finally polished with SiC papers from 500 to 4000 grit.
- SMATed samples at Room Temperature (SMAT-RT): these samples were prepared in the same way as P samples and were SMATed at room temperature.
- SMATed samples at Cryogenic Temperature (SMAT-CT): these samples were prepared like the P samples and were SMATed at cryogenic temperature.

Table 1 gives the different treatment conditions with their corresponding temperature variations during SMAT as well as the resulting surface roughness. The temperature was probed with thermocouples placed in holes drilled from one sample head to the central section along the longitudinal axis of some samples that were used only for that matter. For SMAT at room temperature, the sample core temperature rose from 20°C to about 80°C, due to the heat generated by the shot impacts, before reaching a steady state after about 2 min. The samples treated at cryogenic temperature were first cooled down to -170°C

with liquid nitrogen and were subsequently SMATed. Their core temperature increased by roughly the same amount to about -100°C before stabilizing after less than 4 min.

2.2. Microstructure and surface analyses

The linear surface roughness was measured along the longitudinal axis on the central section with an average of 6 measurements per sample made with a stylus surface profilometer which had a standard radius of 5 μm.

Microstructural observations were made on mirror-polished cross-section surfaces cut perpendicularly to the longitudinal axis of the samples. Scanning Electron Microscopy (SEM) images were acquired with an acceleration voltage of 20 kV and an aperture size of 90 μm with a Supra 40 apparatus. The working distance was either 18 mm on fracture surfaces or 10 mm for other SEM observations. A Symmetry detector and the Aztec software from Oxford Instruments were used for the Electron BackScattered Diffraction (EBSD) mappings. EBSD mappings were acquired with an acceleration voltage of 10 kV for a working distance of 15 mm, a scanning step size of 300 nm and an aperture size of 60 μm.

The gradient of the phases present in the surface and subsurface microstructures was measured using $\theta - 2\theta$ X-Ray Diffraction profiles acquired during 10 min with a 2D detector on a Bruker D8 apparatus. A Co K_α source was used with a 40 kV tension and a 30 mA current. It should be noted that the gradients obtained from these measurements are only qualitative since the present Co K_α radiation had a penetration depth of about 30 μm in titanium [54]. As such, the XRD profiles measured are significantly affected by the phases within the first 30 μm below the measured surface. The profiles were obtained after successive electro-polishing using an electrolytic solution composed of: 6% acid, 35% butoxyethanol and 59% methanol, and a tension of 24 V. A silicone mask was used to select and limit the electropolished surface of the sample. A numerical micrometer was used to measure the removed depth after each polishing step. The cylindrical samples were rotated at 20 rpm along the longitudinal direction to increase the number of diffracting grains during the XRD profile measurement. The background noise of the diffraction spectra was approximated by a 6^{th} degree polynomial expression and subtracted to the measured XRD

profiles. To emerge from the background noise, the volume fraction of a given phase needs to be higher than 5%.

Vickers microhardness profiles were acquired with a 25 g load on the cross-sections observed by SEM. The measurements started at 30 μm below the surface and continued every 30 μm toward the core. The profiles were obtained from an average of 10 measurements.

The residual stress profiles were acquired with a μ-X360s Pulstec apparatus using a vanadium source and the cos α method [55]. The residual stresses profiles were made after successive electro-polishing on fatigue samples - similarly to the $\theta - 2\theta$ XRD profiles - along the longitudinal axis. In order to significantly increase the number of diffracting grains and improve the reliability of the measurements, the samples were rotated at a speed of 20 rpm for the residual stresses measurements which lasted 1 min. The effects of surface material removal on the residual stresses were corrected according to Moore et al. as the geometry of the pocket allows the proposed simplifications [56].

2.3. Fatigue and failure analyses

Four points rotative bending fatigue tests were conducted with an R. R. Moore test apparatus at a rotating frequency of 30 Hz ($R = -1$). The samples were loaded to given stress levels for an intended fatigue life below 10^6 cycles. Due to the limited number of samples for each condition, a staircase method was used. Run-out samples were tested again with an increased load by increments of 20 MPa. The result of the new test was considered valid only if failure occurred after 100 000 cycles. The run-outs with the highest value are also plotted on the fatigue graph and retested samples are identified by an R letter at the bottom right of the corresponding symbol using the same color.

After fracture, tomography measurements were carried out on the regions located below the fracture surfaces with a XT H 225 apparatus from Nikon Metrology in order to detect large subsurface fractures in these regions and to determine their shapes. The acquisition was made with a tension of 210 kV, an intensity of 43 μA and an exposure time of 1 s per projection for a total of 2634 projections. The apparatus had a resolution of 3.96 μm in this configuration. The acquired data were processed with the Dragonfly software.

3. Results

This section is divided into four different subsections dealing with the deformed microstructure, the surface properties, the fatigue properties and, lastly, analyses of the fracture surfaces.

3.1. Deformed Structure Analyses

SEM observations allow to show the initial microstructure of the material and the subsequent effects of the two types of SMAT processing. Fig. 2a is a SEM micrograph of the core microstructure at a low magnification and reveals large β grains of about 260 μm. Figs. 2b and c present band contrast images obtained from EBSD mappings along the cross-section at the surface of the SMAT-RT and SMAT-CT samples, respectively. The band contrast displays the quality of the indexation of EBSD patterns and it is represented by shades of grey, with white being the best and black showing points where the indexation failed. The indexation can be improved by better regularity of the crystallographic cell (less structural defects like dislocations, for example). Deformation bands of different widths and oriented along different directions were formed. For both SMATed samples, these deformation bands are present from the surface down to a depth of about 200 μm but they are mainly present within the first 100 μm. The SMAT-RT samples (Fig. 2b) show a narrow range of band widths and a homogeneous distribution around an average width. The SMAT-CT samples (Fig. 2c) display a larger range of deformation band widths. Some are extremely thick while others are significantly thinner, and the band widths are not homogeneously distributed over this range. Instead, both extremes of this range are considerably more common than the rest. Surprisingly, both SMAT-RT and SMAT-CT samples band contrast mappings show a microstructure at the top surface with a better indexation rate and a lower deformation band density compared to the microstructure deeper in the material (Fig. 2b and c). This effect is particularly visible for SMAT-CT samples as the deformation bands are less dense at the top surface. The deformation at the extreme surface was not significant enough to generate a nanostructure which allowed such a high indexation rate.

In order to understand the nature of these deformation bands, more observations are needed. Figs. 3a and b represent the inverse pole figures (IPF) maps extracted from the same EBSD mappings shown in Fig. 2 for the SMAT-RT (3a) and SMAT-CT (3b) samples, respectively. The indexation rate drops significantly in the bands due to the significant deformation. The IPF only provides information concerning the changes in crystallographic orientation for the large deformation bands as the smallest ones visible in Figs. 2b and c were thinner than the 300 nm stepsize. A zoom on the region marked by a red rectangle in Fig. 3a is shown in Fig. 3c. The high indexation rate due to the lower deformation at this depth allows the identification of the deformation bands characteristics. The cumulative misorientation variation across the deformation bands was determined for four of these bands along the lines labeled A to D and was represented in Fig. 3d. The misorientations between the bands and their surroundings vary between 5° and 24°. Interestingly, the A and D lines cross two bands aligned in the same direction but they present different misorientation variations. The D-line presents a progressive misorientation variation through the entire band whereas the A-line variation is far steeper at the edges of the band while it is constant at its center. The pole figures of the regions around the A and C lines are given in Fig. 3e and f, respectively. Fig. 3e displays the {541} poles while the Fig. 3f shows the {110} poles. On both figures, a rotation around one pole, indicated by the circles in dashed lines, can be observed. All these characteristics indicate that these deformation bands are actually kink bands as depicted in detail by Zheng et al. [43].

The effects of SMAT on the martensitic transformation in the 5553 β-metastable titanium alloy can be determined thanks to XRD techniques. Figs. 4a and b give XRD profiles, respectively on the SMAT-RT and SMAT-CT samples, that were obtained at different depths after successive electro-polishing and they permit to determine the evolution of the phases presence depending on the depth. The depth of each measurement can be seen on the right y-axis at the baseline level of each profile. Notable β and α" peaks are indicated. Zooms on the $\beta(110)$ and α"(111) peak positions are displayed in Figs. 4c and d for SMAT-RT and SMAT-CT, respectively. On both SMATed samples, no martensite is detected at the surface. The α"(111) peak begins to appear after the first electro-polishing at a depth of

15 μm for the SMAT-RT and SMAT-CT samples. Between 30 and 60 μm, the martensite peak is clearly visible for both sample conditions. For the SMAT-RT sample, the peak is barely visible at 80 μm and disappears at further depths. For the SMAT-CT sample, the martensite can be detected down to 120 μm. The appearance of only a single well-defined peak prevents an accurate quantification of the martensitic phase. The other peaks are covered by the background noise. However, the fact that the martensite α"(111) peak is visible means that the volume fraction of martensite should be at least about 5%. Thus, the formation of martensite was promoted when the treatment was carried out at cryogenic temperature and the transformation was lower at the surface compared to the subsurface.

3.2. Surface and Subsurface Properties

Since the surface integrity is of major importance in high-cycle fatigue due to the promotion of surface cracks for low integrity, determining the surface roughness is mandatory. Table 1 displays the Ra and Rz parameters of the surface roughness for polished and SMATed samples. The SMAT-RT surface samples present a roughness about 4 times higher compared to the SMAT-CT surface condition due to the increased mechanical strength of materials at cryogenic temperature leading to a lower deformation of the surface for a given imparted energy of the shots.

Hardness measurements allow to determine the effectiveness of SMAT in reinforcing the considered surfaces by severe plastic deformation. Fig. 5a gives the hardness evolutions as a function of the depth from the surface in the SMAT-RT and SMAT-CT samples. The SMAT-RT sample shows an increase in hardness of about 15% whereas the SMAT-CT presents only a 9% increase, at 30 μm below the surface. The affected depth dropped from 200 μm to 150 μm with the use of the cryogenic temperature.

The residual stresses significantly limit the crack propagation in the regions in compression and as such they significantly impact the fatigue behavior. Fig. 5b displays the residual stress profiles for both SMAT-RT and SMAT-CT sample conditions. Both profiles appear extremely similar in shape and intensities. The compressive residual stresses are about -400 MPa at the surface and the residual stress profiles reach a compression peak at a depth

slightly over 100 μm with a value of about -650 MPa for the SMAT-RT samples and -600 MPa for the SMAT-CT samples. The residual stresses then increase until they reach 0 MPa at a depth of about 350 μm.

3.3. Fatigue Properties

The samples were submitted to a stress amplitude for an intended fatigue life between 10^5 and 10^6 cycles. Fig. 6 gives the results of the fatigue tests in the form of the stress amplitude level as a function of the number of cycles to failure for SMAT-RT treated samples (red crosses), SMAT-CT treated samples (blue diamonds) and Polished samples (black circles). Arrows below the marks represent the run-out tests for which the experiments were stopped at the indicated number of cycles. From these results, the Polished and SMAT-RT conditions display similar fatigue resistances. The SMAT-CT condition presents an improvement in the fatigue resistance by about 20 MPa (or about 8%) compared to the other conditions.

3.4. Fracture Surfaces

The observation of fracture surfaces allows to determine how cracks initiated and propagated, thus providing insights into understanding the fatigue behaviors of the studied conditions. Based on the observations made on the fracture surfaces, all samples present subsurface nucleation sites and only the polished samples presented some initiation sites at the surface (not documented below). Figs. 7a, b and c show SEM images of the fracture surfaces, respectively for the Polished, SMAT-RT and SMAT-CT conditions. The analyses of the fracture surfaces are not straightforward, as several primary cracks are found and may propagate over similar distances before merging. The term "primary crack" is used in this context to designates the cracks leading to failure while the term "secondary crack" refers to those found either on the fracture surface or elsewhere in the sample without affecting the failure mechanism. Fig. 7a displays clear pseudo-cleavage features in the region within the black outline. In all conditions, such pseudo-cleavage features are recognizable on the fracture surface and help backtracking to the initial nucleation points on which they converge (identified with red arrows). Higher magnification images of the identified initiation sites

are given in Figs. 7d, e and f, for Polished, SMAT-RT and SMAT-CT samples, respectively. The primary cracks were found to nucleate on subsurface defects and they propagated with a pseudo-cleavage mechanism along preferential planes in their original grain before continuing on to the next grains along other preferential planes with similar orientations. Some ductile fracture features typical of overload can be observed between the pseudo-cleavage regions, indicated by the full black arrows. No fatigue striations were observed. Due to the interaction of different cracks, all initiation sites may not necessarily be present on the fracture surfaces. Some cracks initiated below the fracture surface, indicated by the white arrows. Their importance is unclear and some of them may have been the initiation location of primary cracks. In Fig. 7a, the features on two large pseudo-cleavage regions, pointed by yellow arrows, could not be used to backtrack to their initiation sites, but their origins were clearly disconnected from the initiation site identified with the red arrow. The fact that these large pseudo-cleavages have different origins shows that these primary cracks may independently nucleate and propagate to an important size before merging.

Further observations of the complete fracture surfaces showed a change in fracture mechanisms at the surface of SMATed samples. Fig. 8a displays the complete fracture surface of the SMAT-CT sample presented partially in Fig. 7c. The primary crack initiation site indicated in Fig. 7c is marked with red arrows in Figs. 8a and b. This global image confirms that primary cracks have propagated along preferential planes through successive grains, as described in Fig. 7. A higher magnification image of the primary crack initiation site in Fig. 8b displays a 250 μm large band along the surface that present rough aspects typical of regions formed during the final rupture. The main crack did propagate preferentially toward the sample center, and only later propagated through this band. Similar observations were made on SMAT-RT samples. A close-up observation of this band (Fig. 8c) shows an emerging crack at the boundary between the band and the main primary crack, indicated by the white arrow.

The tomography technique was used to eventually detect in-depth features without having to cut or alter the samples. Due to the resolution limitation, only large cracks can be identified with this method, but Figs. 8d to g show that tomography analyses can reveal

the presence of the emerging crack between the band and the primary crack (Fig. 8c). The opening of the crack was magnified for the sake of visibility. Figs. 8e to g show the same region in transparency and display a crack network where an enclosed large secondary crack can be found. This crack initiated at a depth of about 250 μm and propagated roughly parallel to the surface main fracture as highlighted in red in Fig. 8f. A bridging that may have appeared during the final fracture (highlighted in white in Fig. 8f) joins this secondary crack to the fracture surface.

4. Discussion

The results, previously reported for the β-metastable titanium alloy, have shown the effects of the SMAT processing conditions and, in particular, the effect of the SMAT temperature. The effects of SMAT on (i) the microstructure and on (ii) the fatigue properties will be discussed successively in the following sections.

4.1. Deformed microstructure

The present results point out that the formation of kink bands is the main deformation mechanism for the SMATed 5553 titanium alloy under the present SMAT loading conditions. The martensitic transformation was concomitant with the kink band formation, as this phase appears within these bands. The presence of kink bands is consistent with observations done in few studies conducted on titanium alloys deformed by a split-Hopkinson pressure bar system (strain rate of $5 \times 10^3\ s^{-1}$). Zheng et al. focused on the Ti-35V-15Cr-0.3Si-0.1C titanium alloy [43] and Qin et al. worked on the 5553 alloy [45]. The appearance of kink bands in the 5553 alloy after SMAT in the present study, but not after shear punching at strain rate up to 200 s^{-1} in [51] nor in compression tests at strain rates of $10^{-3}\ s^{-1}$ in [36] and $0.7 \times 10^{-3}\ s^{-1}$ in [50], tends to support the hypothesis that their formation is promoted at very high strain rates. A strain rate above 200 s^{-1} seems necessary for their formation in the 5553 titanium alloy. According to the calculation of Chan et al. [57] on steel, typical SMAT strain rate can be above $10^3\ s^{-1}$ within the first 300 μm from the surface. However, the local deformation conditions under SMAT did not induce the appearance of adiabatic

shear bands; as noted in the case of split-Hopkinson pressure bar system for similar strain rates [43, 45]. The progressive misorientation seen in the pole figure in Fig. 3e by a gradual rotation of the {541} poles around the circle in dashed red lines illustrates what Zheng et al. have proposed as a mechanism for kink bands formation in β titanium alloys [43]. The kink bands are formed by the migration of edge dislocations in dislocation walls along the slip modes: $\{112\}\langle 111\rangle$, $\{123\}\langle 111\rangle$, $\{101\}\langle 111\rangle$. They show a rotation of the crystal respectively around the three rotation axes, also called Taylor axes: $\langle 110\rangle, \langle 541\rangle, \langle 121\rangle$. The difference in kink band misorientations measured along the A line (A kink band) and D line (D kink band) in Fig. 3d also highlights the hypothesis that kink bands are formed progressively by an accumulation of dislocations in dislocation walls. The D kink band had just begun its formation with a misorientation of 7° while the A kink band is already well formed with a misorientation of 24°. Interestingly, the kink band that is still forming (D) presents a gradual variation of misorientation, compared to the sharp variation of the well-formed kink bands (A).

The fact that the density of kink bands is higher in the subsurface compared to the surface (Figs. 2b and c) can be explained by complementary mechanisms. Firstly, an important part of the dislocations formed close to the surface have the possibility to be annihilated by migrating and reaching the surface; comparatively, the dislocations formed deeper in the subsurface block and interact with each other in order to minimize the stored energy. Secondly, a higher dislocation density is formed in the subsurface due to the location of the higher amplitude of the Hertz stress during impact tests [22, 58]. For a given impact energy of the SMAT, the SMAT-CT condition appears to result in a lower density of large-sized kink bands compared to the SMAT-RT condition. The increase in yield strength at cryogenic temperature, resulting from a decreased mobility of dislocations, reduces the number of dislocations formed after each impact. The distance between the dislocations should allow them to move without immediately interacting and pinning each other down in dense dislocation walls or dislocation entanglements, as would be the case for the SMAT at room temperature. Thus, the mean free path of dislocations should be higher for the SMAT at cryogenic temperature. The dislocations more easily migrate to form fewer but larger

kink bands, albeit at a slow velocity due to the low temperature, increasing their size and resulting in the appearance of the largest kink bands (Fig. 2c). The multitude of thinner kink bands formed for SMAT-RT is a testimony of the low mean free path of dislocations at this temperature (Fig. 2b).

SMAT allowed the formation of martensite only within the kink bands in the subsurface. While no martensite was detected at the surface for both SMAT-RT and SMAT-CT, it was visible on the XRD profiles deeper in the subsurface suggesting that the volume fraction of martensite was higher than 5% in the subsurface. The cryogenic temperature improved the ability to trigger the martensitic transformation as lower temperature result in the presence of martensite deeper in the subsurface. This easier martensitic transformation within the kink bands may interact with the dislocation walls at the interface between the kink bands and their surroundings, forcing them apart and expanding them beyond the size they would reach otherwise. This hypothesis could potentially explain why the thickest kink bands were obtained for SMAT-CT samples. However, the ability of the martensitic transformation to assist the formation of kink bands remains to be understood.

Under the present processing parameters, no ultrafine grains were observed at the top surface after SMAT at both RT and CT showing that the processing condition was mild. Instead, the microstructure at the top surface was fragmented only by the kink bands. We have found that the fragmentation process continues and results in the formation of a nanostructure when the SMAT duration increased to several hours, the SEM images used for this observation are not given here as the relevance to add them as a new figure is minimal. However, the SMAT duration that was already 40 min long in the present case should be increased to several hours to generate similar nanostructures, which may not be practical for industrial applications as it would add high manufacturing costs (low production rate and rapid wear of SMAT equipment). Besides, in the present study, the goal was to investigate the effects of the SMAT temperatures on the fatigue resistance, and not the effects of the SMAT duration. Indeed, it has been demonstrated that an increased SMAT duration leads to a loss of surface integrity, due to the alteration generated by the intensity of the deformation treatment; and negative impact on the fatigue resistance was observed for long treatments

in superalloys, stainless steels and aluminium alloys [13, 19, 20].

It is relevant to compare the effects of SMAT at cryogenic temperature on the present β-metastable Ti alloy to those reported in the case of austenitic stainless steels [21, 22]. In the work done by Novelli et al. as well as in the present work, the SMAT-CT seems to significantly promote the martensitic transformation as less stress and deformation are necessary to trigger the transformation at the low temperature. Both works also show that SMAT-CT allows to significantly reduce the roughness due to the increase in mechanical strength of materials at cryogenic temperature which induces a lower surface deformation for the same energy provided by the shots. However, the present SMAT-CT condition on the 5553 alloy displays less surface hardening compared to the SMAT-RT condition, providing quite different results from these reported by Novelli et al. [21, 22]. Indeed, Novelli et al. showed that using SMAT at CT could significantly increase the subsurface hardness over a larger depth range compared to SMAT at RT thanks to the promoted formation of hard martensite with a significant volume change during the transformation. The low volume change during the α" martensitic transformation in titanium limit the martensitic hardening in these alloys.

4.2. Impact on fatigue

The fatigue behavior of the present 5553 alloy is extremely dependent on crystallographic features, both in the initiation of fatigue cracks and in their propagation.

The fracture surfaces are rather difficult to read and interpret (Fig. 7), but according to the observations gathered on all broken samples, a primary crack appeared in a subsurface grain and started to propagate through the grain along a preferential plane. As the primary crack reached the grain boundary, it spread through the next grain along another preferential plane with similar orientation. Additionally, the crack reduced the local load-carrying capability and thus increased the stress concentration of the neighboring region. Several cracks nucleated and propagated according to the same pattern and once the load-carrying capability reached a critical level, secondary cracks started to bridge the gaps between already fractured regions, leading to the failure.

The initiations mainly started at subsurface defects, such as triple junctions, for all sample conditions, i.e. polished and SMATed samples. For the polished samples, the low surface roughness and early surface plasticity were apparently less detrimental than some subsurface defects as main initiations are located in the subsurface. For SMATed surfaces, the initiations appeared at a depth over 250 μm from the surface which corresponds to the depth where the compressive residual stresses contribution is relatively low. For the SMATed samples, cracks only propagated toward the surface during the final stage of the crack propagation as they have to go through the region with high compressive residual stresses. This may result in the increase in the number of cycles to failure.

Despite SMAT producing an increased surface hardness and important compressive residual stresses, the SMAT-RT samples had similar fatigue resistances to that of Polished ones. This is surprising since the cracks on Polished samples could easily reach the surface and propagate more rapidly to a critical size. The propagation for the SMAT-RT was prevented in the 250 μm layer from the surface during the initial propagation stage, as such the crack could only grow to the critical size by propagating toward the center of the samples, where the stress amplitude is lower. From these observations, the SMAT-RT should have a fatigue resistance noticeably higher than that of the Polished samples. Maybe the high surface roughness of SMAT-RT samples acted as stress concentrators and helped the crack in propagating through the hardened layer in compression, thus reducing the critical crack size needed before the final fracture. This hypothesis may also explain why SMAT-CT condition produced an 8% increase in fatigue resistance as the surface roughness was significantly lowered, even if these samples also presented a lower hardness and a lower kink band density compared to SMAT-RT samples. Another hypothesis that may explain the better fatigue resistance of SMAT-CT samples is the presence of martensite deeper in the subsurface and of the largest kink bands as both characteristics may also hinder the crack propagation through the deformed layer.

5. Conclusions

The main goal of this study was to investigate the effects of Surface Mechanical Attrition Treatment (SMAT), in particular at cryogenic temperature, on a β-metastable 5553 titanium alloy and the impact on its fatigue properties. The main results can be summarized as follows:

- Kink bands were formed after SMAT in the 5553 β-metastable titanium alloy at its full β state due to the local high strain rates induced by SMAT. The random impact directions, inherent in the SMAT process, allowed the activation of different kink band systems. The kink band density was the highest in the subsurface for both SMAT at room (RT) and at cryogenic temperature (CT).

- The formation of martensite was observed within the kink bands for all SMAT conditions due to the concentration of the deformation in these regions.

- SMAT at cryogenic temperature allowed the formation of martensite deeper in the subsurface compared to SMAT done at room temperature. Contrary to what was observed in some austenitic stainless steels [21, 22], this higher amount of martensite was not associated with an increase in subsurface hardness. On the contrary, the SMAT-CT samples were found softer than the SMAT-RT ones when subsequently tested by micro-hardness at room temperature.

- The roughness after SMAT was reduced by a factor of 4 when the treatment was done at cryogenic temperature compared to the treatment done at room temperature due to the increased mechanical strength of the alloy at lowest temperature of SMAT processing.

- SMAT-CT resulted in an improvement of the fatigue resistance by 8% compared to the SMAT-RT. Two hypotheses may explain this difference: (i) the deeper martensite and the largest kink bands formed by SMAT-CT may have delayed the final fracture; and (ii) the high roughness produced by SMAT-RT may have introduced stress raisers

at the surface. As these two hypotheses are not in contradiction with each other, a combination of both may be possible.

- Surprisingly, SMAT-RT and polished samples both had similar fatigue resistance. The core microstructure in the investigated condition of the 5553 alloy presented significant crystallographic defects due to its large grain size and this resulted in the weakest region for fatigue being located in the subsurface. Consequently, the impact on fatigue of the surface features induced by SMAT - such as martensite, kink bands and compressive residual stresses - was limited. Additionally, if the second hypothesis presented above is true, the significant surface roughness may have reduced the effectiveness of the compressive residual stresses induced by SMAT.

Acknowledgements

The authors would like to acknowledge Dr. Antoine Guitton, Dr. Marc Novelli, Dr. Dorian Delbergue and Dr. Sebastien Le Corre for their valuable discussions and insights. The authors are thankful to Mrs. Céline Salomon for proofreading this paper.

Funding: This work was supported by the French Government through the program "Investissements d'avenir" operated by the French National Research Agency (ANR) and referenced to as ANR-11-LABX-0008-01 ('LabEx DAMAS'). This work was also supported by the Laboratory of Optimization of Advanced Processes and Fabrication (LOPFA, Montréal, Canada). The material used in this paper was graciously given by TIMET Savoie, France.

References

[1] T. C. Lowe, R. Z. Valiev, The use of severe plastic deformation techniques in grain refinement, JOM Journal of the Minerals, Metals and Materials Society 56 (10) (2004) 64–68 (2004). doi:10.1007/s11837-004-0295-z.

[2] Y. Estrin, A. Vinogradov, Extreme grain refinement by severe plastic deformation: A wealth of challenging science, Acta Materialia 61 (3) (2013) 782–817 (2013). doi:10.1016/j.actamat.2012.10.038.

[3] I. A. Ovid'ko, R. Z. Valiev, Y. T. Zhu, Review on superior strength and enhanced ductility of metallic nanomaterials, Progress in Materials Science 94 (2018) 462–540 (2018). doi:10.1016/j.pmatsci.2018.02.002.

[4] K. Edalati, Z. Horita, A review on high-pressure torsion (HPT) from 1935 to 1988, Materials Science and Engineering: A 652 (2016) 325–352 (jan 2016). doi:10.1016/j.msea.2015.11.074.

[5] R. Z. Valiev, T. G. Langdon, Principles of equal-channel angular pressing as a processing tool for grain refinement, Progress in Materials Science 51 (7) (2006) 881–981 (sep 2006). arXiv:NIHMS150003, doi:10.1016/j.pmatsci.2006.02.003.

[6] R. L. Murthy, B. Kotiveerachari, Burnishing of metallic surfaces - a review, Precision Engineering 3 (3) (1981) 172–179 (1981). doi:10.1016/0141-6359(81)90010-6.

[7] C. S. Montross, T. Wei, L. Ye, G. Clark, Y. W. Mai, Laser shock processing and its effects on microstructure and properties of metal alloys: A review, International Journal of Fatigue 24 (10) (2002) 1021–1036 (2002). doi:10.1016/S0142-1123(02)00022-1.

[8] X. Wu, N. Tao, Y. Hong, B. Xu, J. Lu, K. Lu, Microstructure and evolution of mechanically-induced ultrafine grain in surface layer of AL-alloy subjected to USSP, Acta Materialia 50 (8) (2002) 2075–2084 (2002). doi:10.1016/S1359-6454(02)00051-4.

[9] K. Lu, J. Lu, Nanostructured surface layer on metallic materials induced by surface mechanical attrition treatment, Materials Science and Engineering A 375-377 (1-2 SPEC. ISS.) (2004) 38–45 (2004). doi:10.1016/j.msea.2003.10.261.

[10] S. Bagheri, M. Guagliano, Review of shot peening processes to obtain nanocrystalline surfaces in metal alloys Review of shot peening processes to obtain nanocrystalline surfaces in metal alloys, Surface Engineering 25 (1) (2009) 3–14 (2009). doi:10.1179/026708408X334087.

[11] J. Azadmanjiri, C. C. Berndt, A. Kapoor, C. Wen, Development of Surface Nano-Crystallization in Alloys by Surface Mechanical Attrition Treatment (SMAT), Critical Reviews in Solid State and Materials Sciences 40 (3) (2015) 164–181 (2015). doi:10.1080/10408436.2014.978446.

[12] A. Heydari, R. Miresmaeili, S. Bagherifard, M. Guagliano, M. Aliofkhazraei, Incorporating the principles of shot peening for a better understanding of surface mechanical attrition treatment (SMAT) by simulations and experiments, Materials & Design 116 (2017) 365–373 (2017). doi:10.1016/j.matdes.2016.12.045.

[13] T. Grosdidier, M. Novelli, Recent Developments in the Application of Surface Mechanical Attrition Treatments for Improved Gradient Structures: Processing Parameters and Surface Reactivity, Materials Transactions 60 (7) (2019) 1344–1355 (jul 2019). doi:10.2320/matertrans.MF201929.

[14] S. Curtis, E. R. De Los Rios, C. A. Rodopoulos, A. Levers, Analysis of the effects of controlled shot peening on fatigue damage of high strength aluminium alloys, International Journal of Fatigue 25 (1) (2002) 59–66 (2002). doi:10.1016/S0142-1123(02)00049-X.

[15] Y. Sun, Sliding wear behaviour of surface mechanical attrition treated AISI 304 stainless steel, Tribology International 57 (2013) 67–75 (2013). doi:10.1016/j.triboint.2012.07.015.

[16] P. Maurel, L. Weiss, P. Bocher, E. Fleury, T. Grosdidier, Oxide dependent wear mechanisms of titanium against a steel counterface: Influence of SMAT nanostructured surface, Wear 430-431 (February) (2019) 245–255 (2019). doi:10.1016/j.wear.2019.05.007.

[17] T. Wang, J. Yu, B. Dong, Surface nanocrystallization induced by shot peening and its effect on corrosion resistance of 1Cr18Ni9Ti stainless steel, Surface and Coatings Technology 200 (16-17) (2006) 4777–4781 (2006). doi:10.1016/j.surfcoat.2005.04.046.

[18] K. D. Ralston, N. Birbilis, Effect of grain size on corrosion: A review, Corrosion 66 (7) (2010) 0750051–07500513 (2010). doi:10.5006/1.3462912.

[19] J. W. Tian, J. C. Villegas, W. Yuan, D. Fielden, L. Shaw, P. K. Liaw, D. L. Klarstrom, A study of the effect of nanostructured surface layers on the fatigue behaviors of a C-2000 superalloy 470 (2007) 164–170 (2007). doi:10.1016/j.msea.2006.10.150.

[20] V. Pandey, K. Chattopadhyay, N. C. Santhi Srinivas, V. Singh, Role of ultrasonic shot peening on low cycle fatigue behavior of 7075 aluminium alloy, International Journal of Fatigue 103 (2017) 426–435 (2017). doi:10.1016/j.ijfatigue.2017.06.033.

[21] M. Novelli, J. J. Fundenberger, P. Bocher, T. Grosdidier, On the effectiveness of surface severe plastic deformation by shot peening at cryogenic temperature, Applied Surface Science 389 (2016) 1169–1174 (2016). doi:10.1016/j.apsusc.2016.08.009.

[22] M. Novelli, P. Bocher, T. Grosdidier, Effect of cryogenic temperatures and processing parameters on gradient-structure of a stainless steel treated by ultrasonic surface mechanical attrition treatment, Materials Characterization 139 (January) (2018) 197–207 (2018). doi:10.1016/j.matchar.2018.02.028.

[23] C. Xin, D. Yang, Q. Sun, L. Xiao, J. Sun, Thermal stability of nanogradient microstructure produced by surface mechanical rolling treatment in Zircaloy-4, Journal of Materials Science (2019). doi:10.1007/s10853-019-04303-z.

[24] T. Grosdidier, Y. Combres, E. Gautier, M. Philippe, Effect of Microstructure Variations on the Formation of Deformation-Induced Martensite and Associated Tensile Properties in a β Metastable Ti Alloy, Metallurgical and Materials Transactions A 31 (April) (2000) 1095–1106 (2000). doi:10.1007/s11661-000-0105-3.

[25] C. Lin, G. Yin, Y. Zhao, P. Ge, Z. Liu, Analysis of the effect of alloy elements on martensitic transformation in titanium alloy with the use of valence electron structure parameters, Materials Chemistry and Physics 125 (3) (2011) 411–417 (2011). doi:10.1016/j.matchemphys.2010.10.039.

[26] A. Bhattacharjee, S. Bhargava, V. Varma, S. Kamat, A. Gogia, Effect of β grain size on stress induced martensitic transformation in β solution treated Ti – 10V – 2Fe – 3Al alloy, Scripta Materialia 53 (2005) 195–200 (2005). doi:10.1016/j.scriptamat.2005.03.039.

[27] M.-H. Cai, C.-Y. Lee, Y.-K. Lee, Effect of grain size on tensile properties of fine-grained metastable b

titanium alloys fabricated by stress-induced martensite and its reverse transformations, Scripta Materialia 66 (2012) 606–609 (2012). doi:10.1016/j.scriptamat.2012.01.015.

[28] T. Grosdidier, C. Roubaud, M.-J. Philippe, Y. Combres, The deformation mechanisms in the β-metastable β-Cez titanium alloy, Scripta Materialia 36 (1) (1997) 21–28 (1997). doi:10.1016/S1359-6462(96)00341-7.

[29] C. Li, X. Wu, J. H. Chen, S. V. D. Zwaag, Influence of α morphology and volume fraction on the stress-induced martensitic transformation in Ti–10V–2Fe–3Al, Materials Science and Engineering A 528 (2011) 5854–5860 (2011). doi:10.1016/j.msea.2011.03.107.

[30] J. I. Kim, H. Y. Kim, T. Inamura, H. Hosoda, S. Miyazaki, Shape memory characteristics of Ti–22Nb–(2–8) Zr (at.%) biomedical alloys, Materials Science and Engineering A 403 (2005) 334–339 (2005). doi:10.1016/j.msea.2005.05.050.

[31] S. Miyazaki, H. Y. Kim, H. Hosoda, Development and characterization of Ni-free Ti-base shape memory and superelastic alloys, Materials Science and Engineering A 440 (2006) 18–24 (2006). doi:10.1016/j.msea.2006.02.054.

[32] T. Grosdidier, M. J. Philippe, Deformation induced martensite and superelasticity in a β-metastable titanium alloy, Materials Science and Engineering A 291 (1) (2000) 218–223 (2000). doi:10.1016/S0921-5093(00)00921-7.

[33] H. Y. Kim, S. Hashimoto, J. I. Kim, H. Hosoda, S. Miyazaki, Mechanical Properties and Shape Memory Behavior of Ti-Nb Alloys, Materials Transactions 45 (7) (2004) 2443–2448 (2004). doi:10.2320/matertrans.45.2443.

[34] Y. L. Hao, S. J. Li, S. Y. Sun, R. Yang, Effect of Zr and Sn on Young's modulus and superelasticity of Ti – Nb-based alloys, Materials Science and Engineering A 441 (2006) 112–118 (2006). doi:10.1016/j.msea.2006.09.051.

[35] S. J. Li, T. C. Cui, Y. L. Hao, R. Yang, Fatigue properties of a metastable β-type titanium alloy with reversible phase transformation, Acta Biomaterialia 4 (2) (2008) 305–317 (2008). doi:10.1016/j.actbio.2007.09.009.

[36] P. Barriobero-Vila, J. Gussone, K. Kelm, J. Haubrich, A. Stark, N. Schell, G. Requena, An in situ investigation of the deformation mechanisms in a β-quenched Ti-5Al-5V-5Mo-3Cr alloy, Materials Science and Engineering A 717 (January) (2018) 134–143 (2018). doi:10.1016/j.msea.2018.01.077.

[37] M. Hida, E. Sukedai, C. Henmi, K. Sakaue, H. Terauchi, Stress induced products and ductility due to lattice instability of β phase single crystal of Ti-Mo alloys, Acta Metallurgica 30 (8) (1982) 1471–1479 (1982). doi:10.1016/0001-6160(82)90167-5.

[38] M. Marteleur, F. Sun, T. Gloriant, P. Vermaut, P. J. Jacques, On the design of new b -metastable titanium alloys with improved work hardening rate thanks to simultaneous TRIP and TWIP effects,

Scripta Materialia 66 (2012) 749–752 (2012). doi:10.1016/j.scriptamat.2012.01.049.

[39] N. Sakaguchi, M. Niinomi, T. Akahori, J. Takeda, H. Toda, Relationships between tensile deformation behavior and microstructure in Ti – Nb – Ta – Zr system alloys, Materials Science and Engineering C 25 (2005) 363–369 (2005). doi:10.1016/j.msec.2004.12.014.

[40] W. Xu, K. B. Kim, J. Das, M. Calin, J. Eckert, Phase stability and its effect on the deformation behavior of Ti–Nb–Ta–In/Cr β alloys, Scripta Materialia 54 (2006) 1943–1948 (2006). doi:10.1016/j.scriptamat.2006.02.002.

[41] A. Zafari, X. S. Wei, W. Xu, K. Xia, Formation of nanocrystalline β structure in metastable beta Ti alloy during high pressure torsion: The role played by stress induced martensitic transformation, Acta Materialia 97 (2015) 146–155 (2015). doi:10.1016/j.actamat.2015.06.042.

[42] Y. Zhang, D. Qi, J. Gao, T. Huang, Analysis of kinking in elastoplastic materials with strain-softening behavior, International Journal of Engineering Science 46 (11) (2008) 1077–1086 (nov 2008). doi:10.1016/j.ijengsci.2008.04.008.

[43] Y. Zheng, W. Zeng, Y. Wang, S. Zhang, Kink deformation in a beta titanium alloy at high strain rate, Materials Science and Engineering A 702 (127) (2017) 218–224 (2017). doi:10.1016/j.msea.2017.07.015.

[44] Y. Zheng, W. Zeng, Y. Wang, D. Zhou, X. Gao, High strain rate compression behavior of a heavily stabilized beta titanium alloy: Kink deformation and adiabatic shearing, Journal of Alloys and Compounds 708 (2017) 84–92 (2017). doi:10.1016/j.jallcom.2017.02.284.

[45] D. Qin, Y. Li, The role of microstructure and stress state in dynamic mechanical behavior of Ti-5Al-5V-5Mo-3Cr alloy, Materials Characterization 147 (June 2018) (2019) 421–433 (2019). doi:10.1016/j.matchar.2018.11.022.

[46] S. Sadeghpour, S. Abbasi, M. Morakabati, L. Karjalainen, Effect of dislocation channeling and kink band formation on enhanced tensile properties of a new beta Ti alloy, Journal of Alloys and Compounds 808 (2019) 151741 (2019). doi:10.1016/j.jallcom.2019.151741.

[47] L. Weiss, Y. Nessler, M. Novelli, P. Laheurte, T. Grosdidier, On the use of functionally graded materials to differentiate the effects of surface severe plastic deformation, roughness and chemical composition on cell proliferation, Metals 9 (12) (2019). doi:10.3390/met9121344.

[48] J. B. Hess, C. S. Barrett, Structure and nature of kink bands in zinc, JOM 1 (9) (1949) 599–606 (sep 1949). doi:10.1007/BF03398902.

[49] M. Yamasaki, K. Hagihara, S. I. Inoue, J. P. Hadorn, Y. Kawamura, Crystallographic classification of kink bands in an extruded Mg-Zn-Y alloy using intragranular misorientation axis analysis, Acta Materialia 61 (6) (2013) 2065–2076 (2013). doi:10.1016/j.actamat.2012.12.026.

[50] S. Sadeghpour, S. M. Abbasi, M. Morakabati, A. Kisko, L. P. Karjalainen, On the compressive deformation behavior of new beta titanium alloys designed by d-electron method, Journal of Alloys and

628 Compounds 746 (2018) 206–217 (2018). doi:10.1016/j.jallcom.2018.02.212.
629 [51] A. Zafari, K. Xia, Grain refinement in a metastable beta Ti alloy deformed to large strains at high
630 strain rates, Acta Materialia 157 (2018) 174–185 (2018). doi:10.1016/j.actamat.2018.07.030.
631 [52] A. K. Elshennawy, G. S. Weheba, Manufacturing processes & materials, Society of Manufacturing
632 Engineers (SME), 2015 (2015).
633 [53] SONATS Europe Technologies Group. (2019, Decembre, 6).
634 URL https://sonats-et.com/en/shot-peening/what-is-shot-peening/
635 [54] B. D. Cullity, Elements of X-ray Diffraction, Addison-Wesley Publishing, 1956 (1956).
636 [55] D. Delbergue, D. Texier, M. Lévesque, P. Bocher, Diffracting-grain identification from elec-
637 tron backscatter diffraction maps during residual stress measurements: A comparison between
638 the sin2w and cosa methods, Journal of Applied Crystallography 52 (4) (2019) 828–843 (2019).
639 doi:10.1107/S1600576719008744.
640 [56] M. Moore, W. Evans, Mathematical correction for stress in removed layers in x-ray diffraction residual
641 stress analysis, SAE transactions (1958) 340–345 (1958).
642 [57] H. L. Chan, H. H. Ruan, A. Y. Chen, J. Lu, Optimization of the strain rate to achieve exceptional
643 mechanical properties of 304 stainless steel using high speed ultrasonic surface mechanical attrition
644 treatment 58 (2010) 5086–5096 (2010). doi:10.1016/j.actamat.2010.05.044.
645 [58] K. L. Johnson, K. L. Johnson, Contact mechanics, Cambridge university press, 1987 (1987).

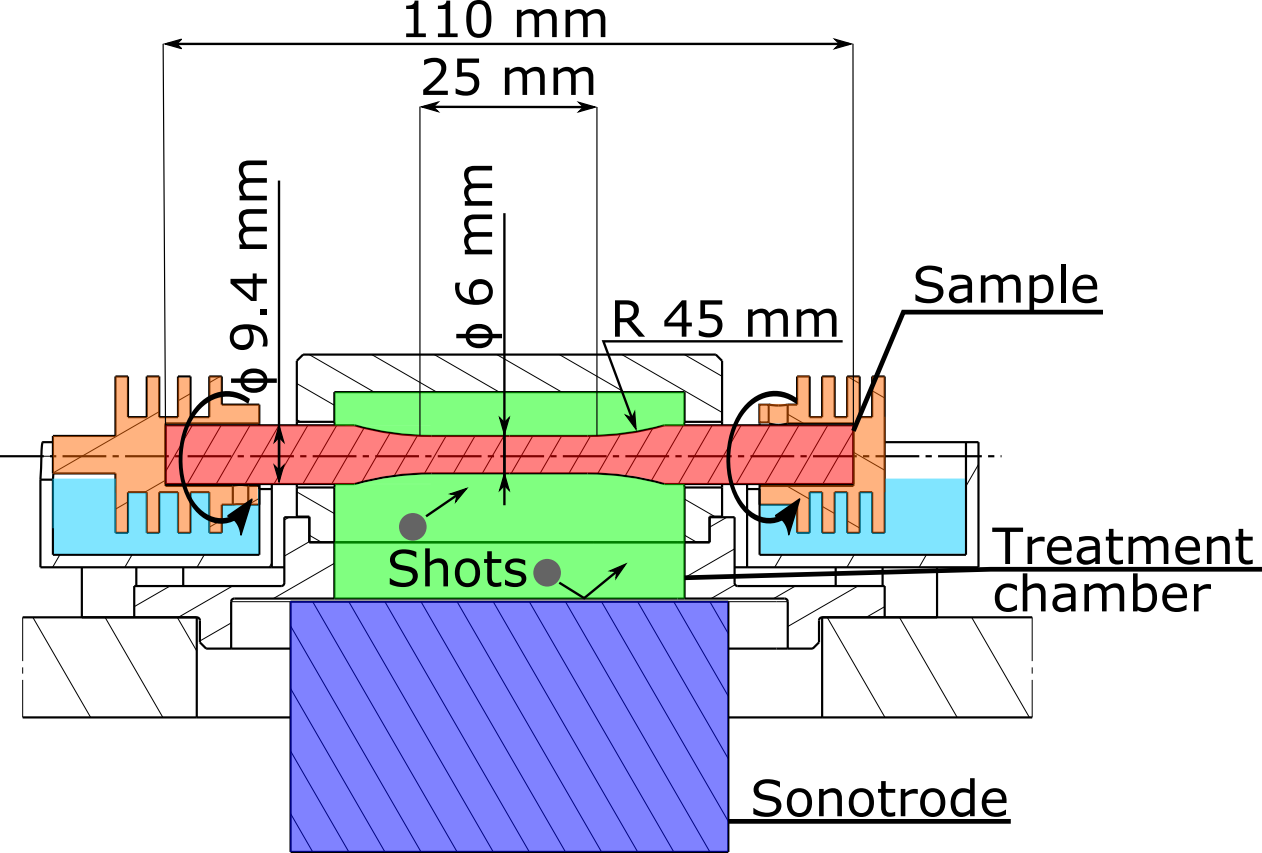
110 mm
25 mm
ϕ 9.4 mm
ϕ 6 mm
R 45 mm
Sample
Shots
Treatment chamber
Sonotrode

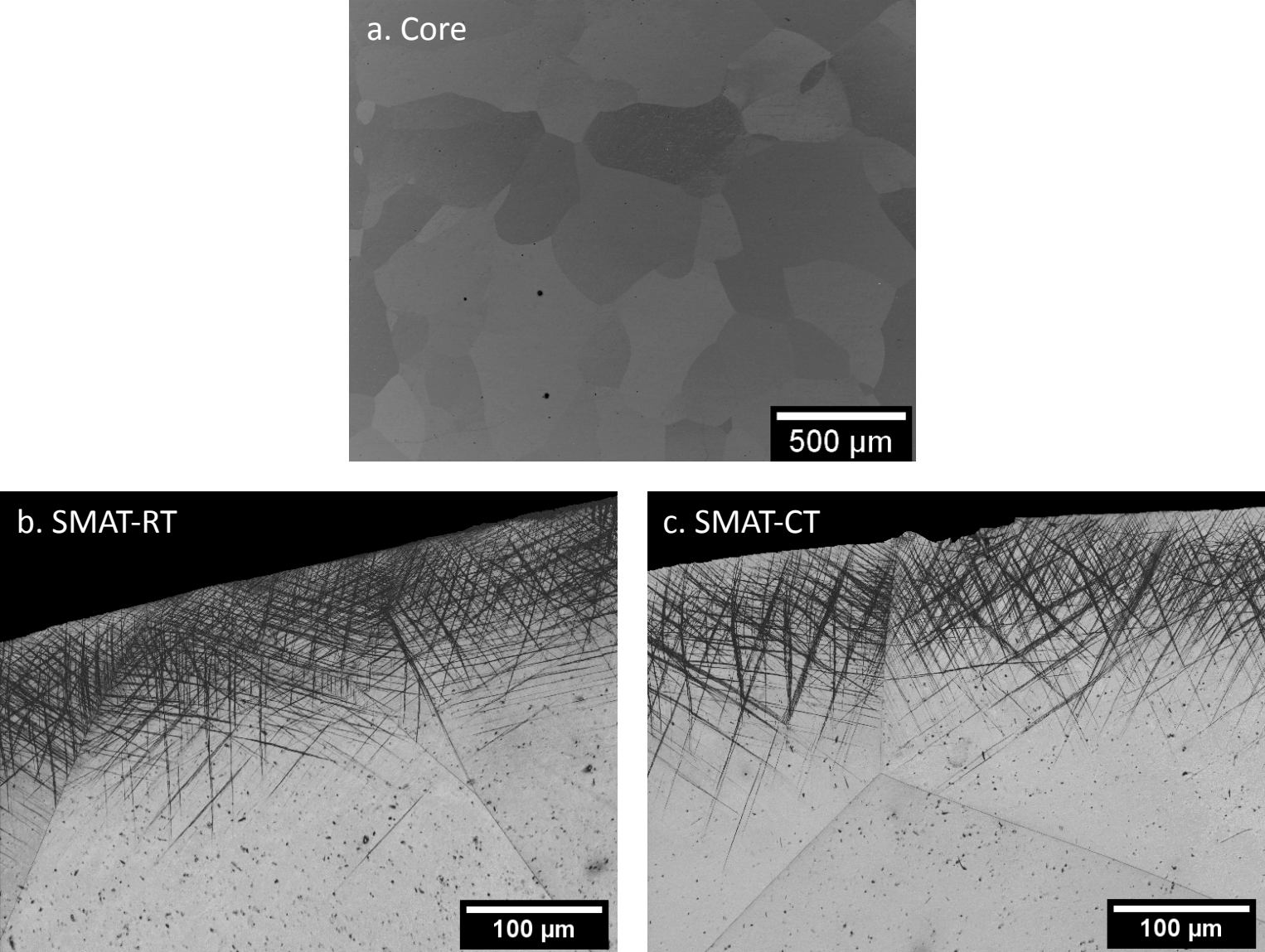
a. Core
500 µm
b. SMAT-RT
100 µm
c. SMAT-CT
100 µm

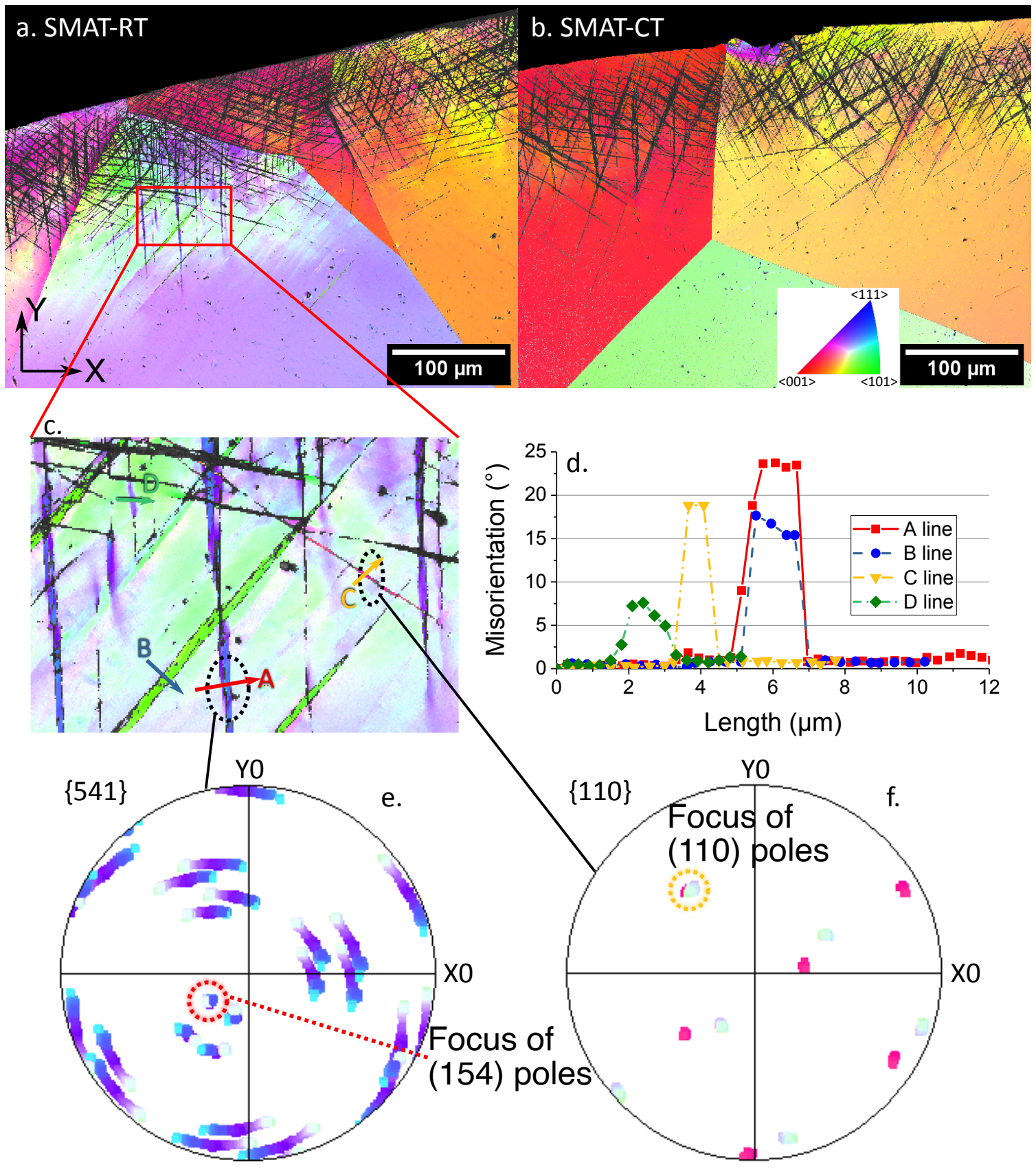
a. SMAT-RT
b. SMAT-CT
Y
X
100 μm
<111>
<001>
<101>
100 μm
c.
D
C
B
A
d.
Misorientation (°)
Length (μm)
A line
B line
C line
D line
{541}
Y0
X0
e.
Focus of
(154) poles
{110}
Y0
X0
f.
Focus of
(110) poles

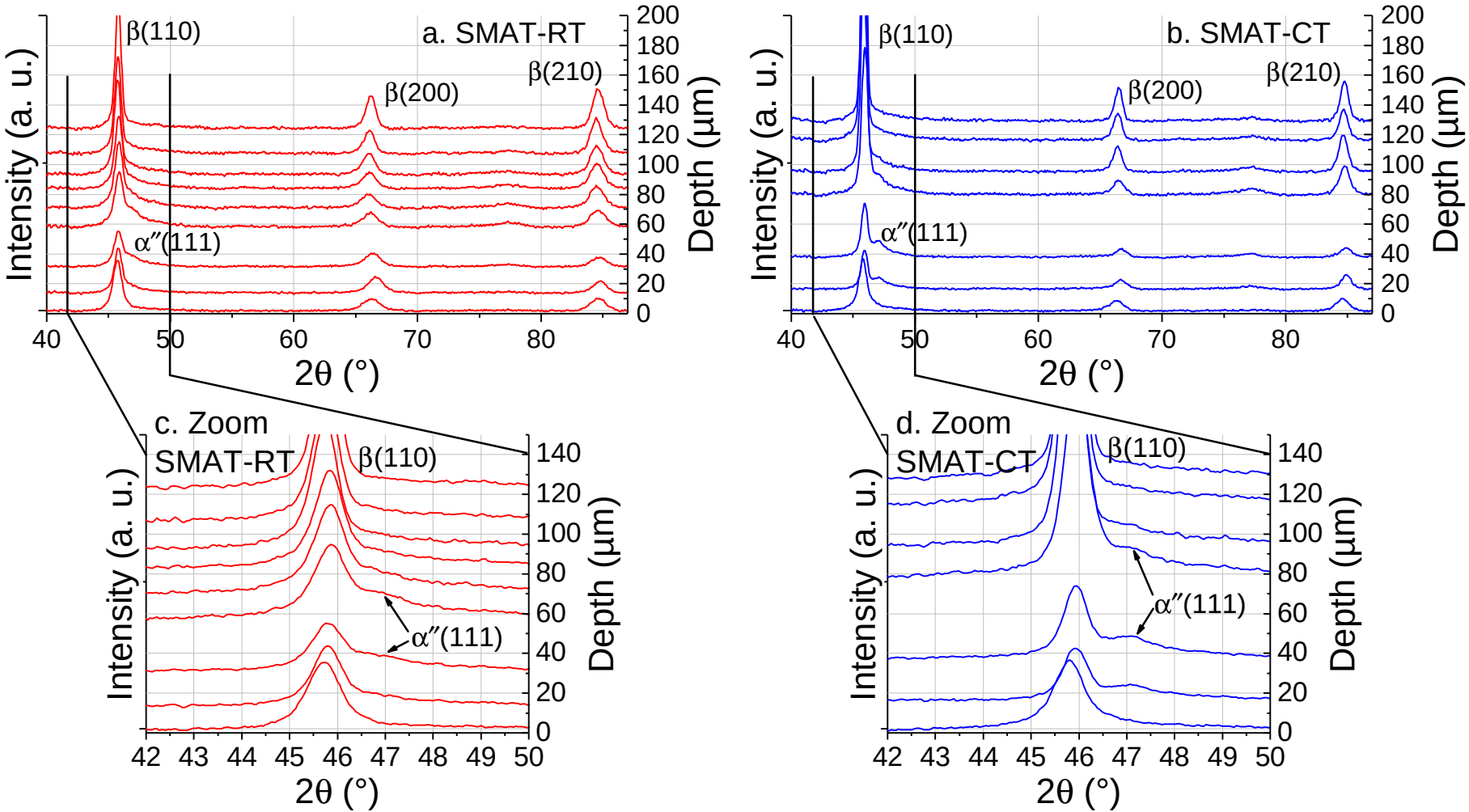
a. SMAT-RT
b. SMAT-CT
c. Zoom
SMAT-RT
d. Zoom
SMAT-CT
β(110)
β(200)
β(210)
α″(111)
Intensity (a. u.)
Depth (μm)
2θ (°)

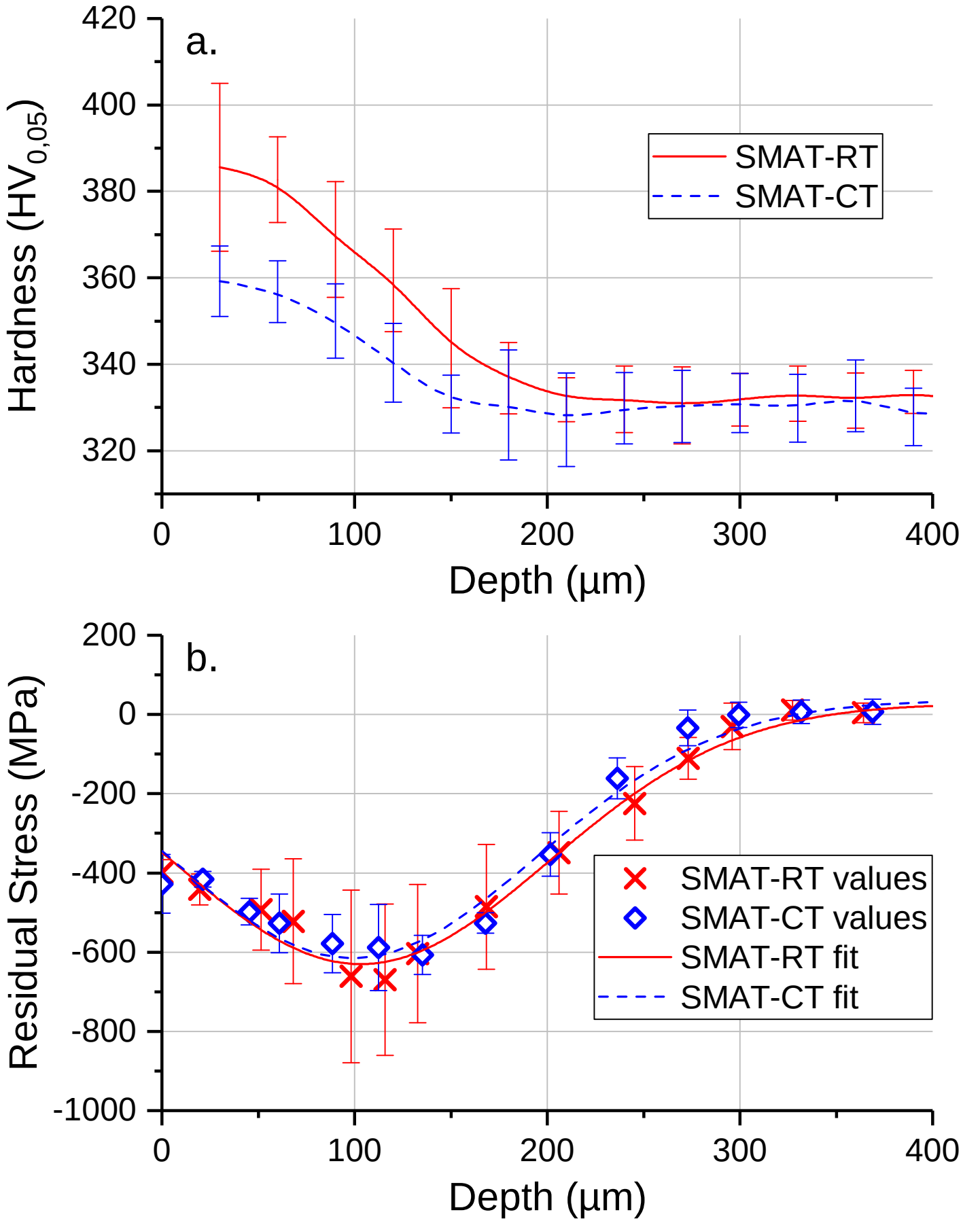
a.
Hardness ($HV_{0,05}$)
420
400
380
360
340
320
0
100
200
300
400
Depth (µm)
SMAT-RT
SMAT-CT
b.
Residual Stress (MPa)
200
0
-200
-400
-600
-800
-1000
0
100
200
300
400
Depth (µm)
SMAT-RT values
SMAT-CT values
SMAT-RT fit
SMAT-CT fit

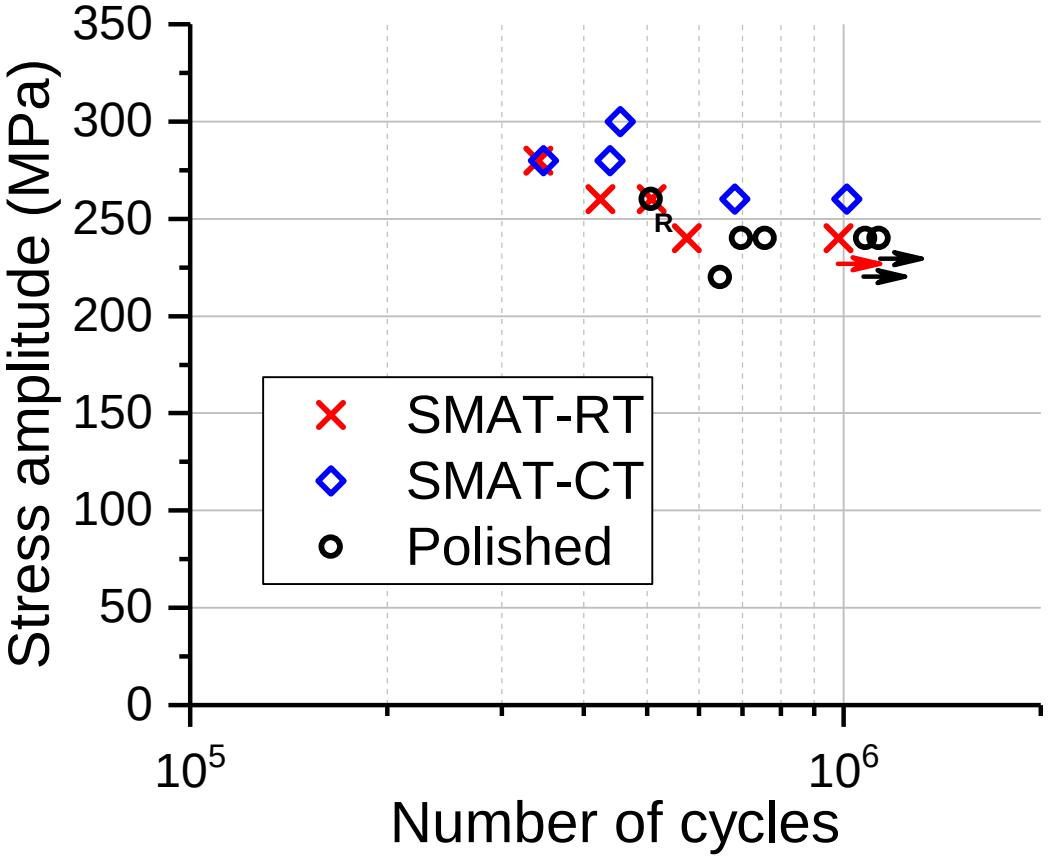
Stress amplitude (MPa)
350
300
250
200
150
100
50
0
10^5
10^6
Number of cycles
SMAT-RT
SMAT-CT
Polished
R

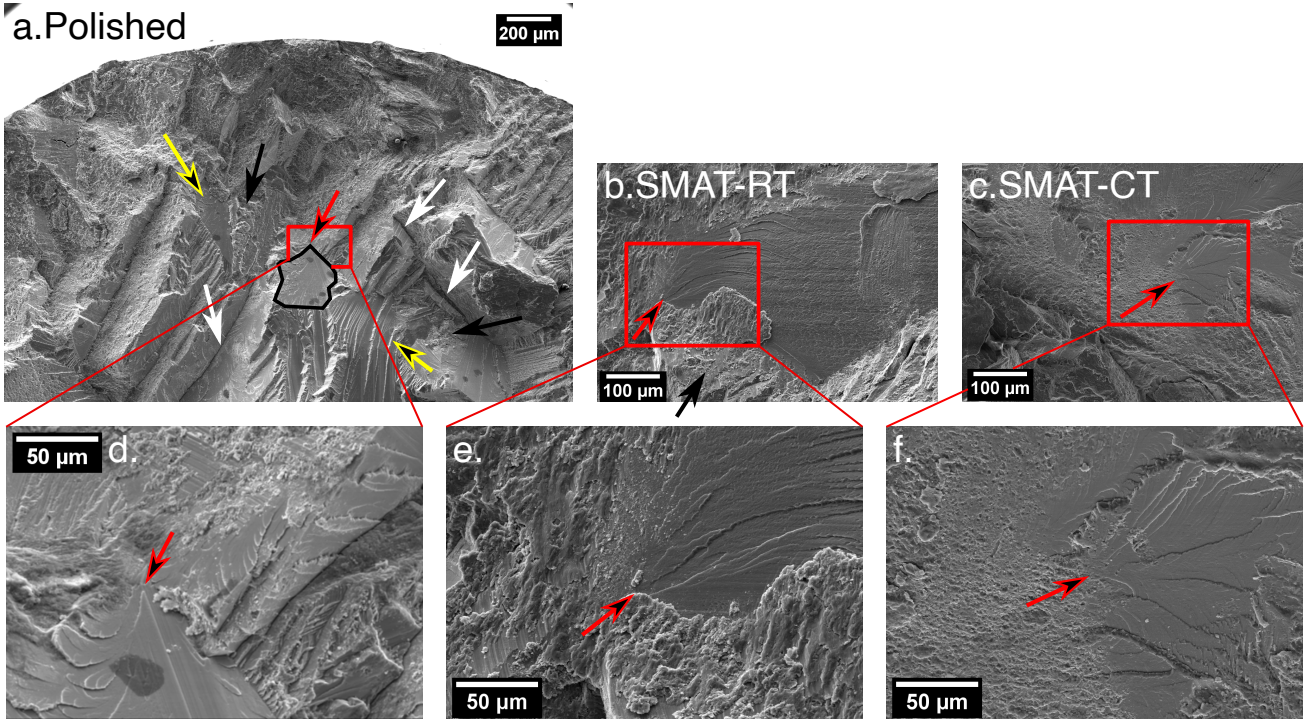
a.Polished
200 μm
b.SMAT-RT
100 μm
c.SMAT-CT
100 μm
50 μm
d.
e.
50 μm
f.
50 μm

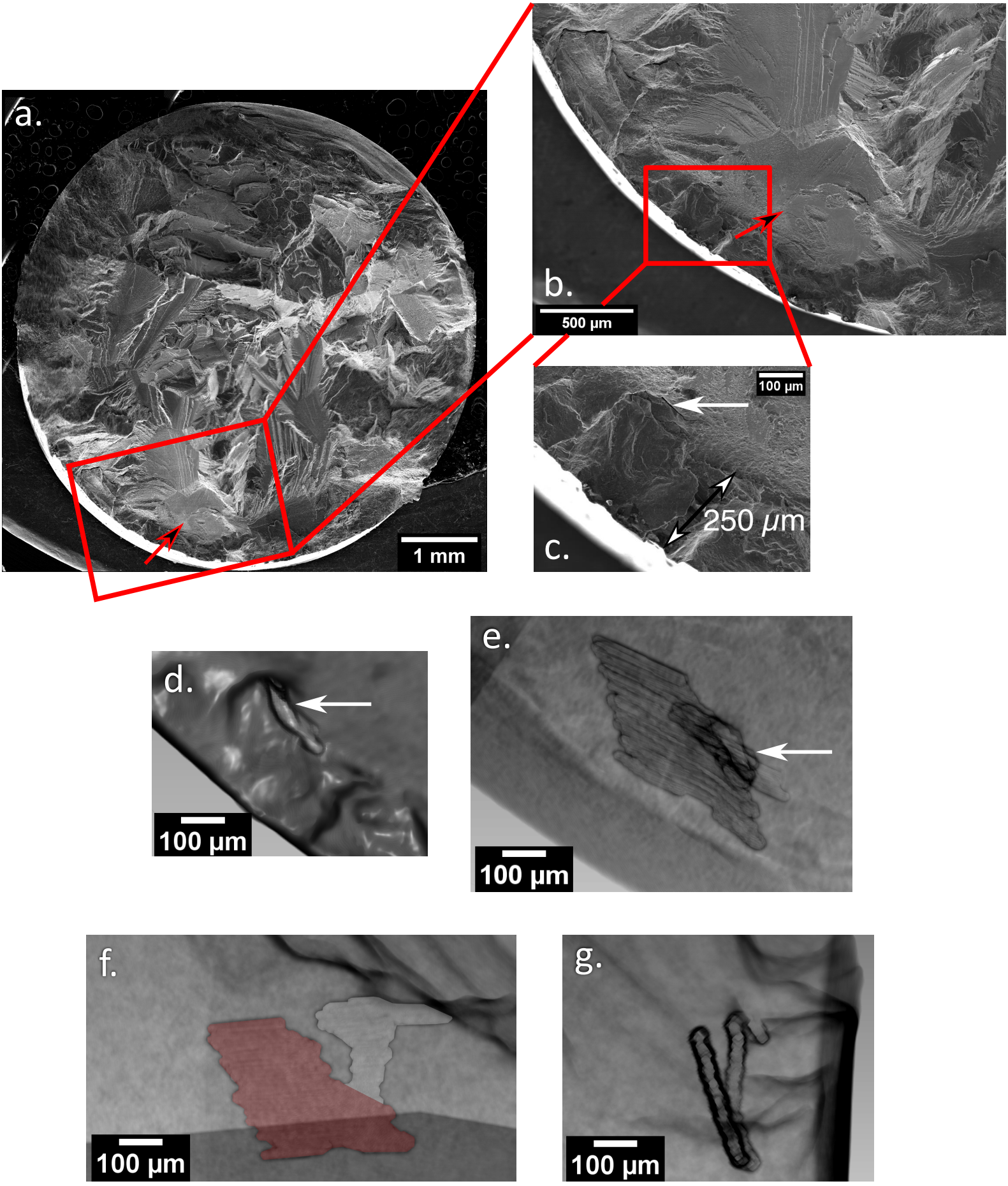
a.
1 mm
b.
500 µm
100 µm
250 µm
c.
d.
100 µm
e.
100 µm
f.
100 µm
g.
100 µm

Sample	Treatment temperature	Ra (μm)	Rz (μm)
Polished (P)	*None*	0.05 ± 0.01	0.34 ± 0.07
SMAT-RT	20 to 80°C	3.13 ± 0.39	14.89 ± 1.75
SMAT-CT	-170 to -100°C	0.81 ± 0.13	3.88 ± 0.64

Table 1: Treatment temperature ranges for SMAT-RT and SMAT-CT samples, Ra and Rz roughness characteristic values.

SMATed microstructures of a β-metastable titanium alloy

Martensitic transformation

Kink band formation

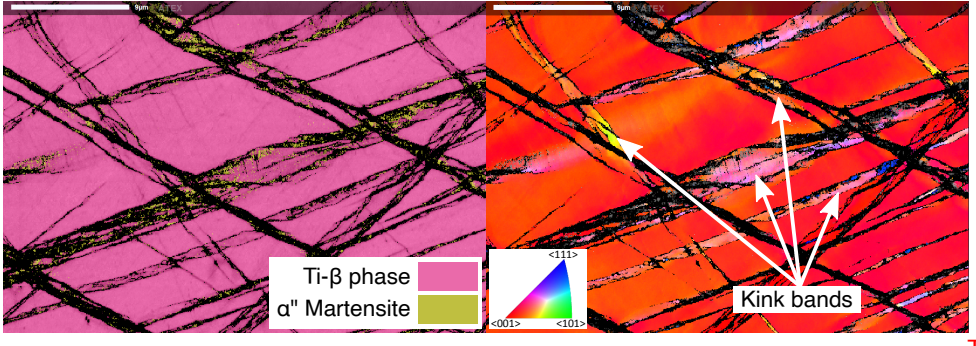

Mechanical properties of SMAT at Cryogenic Temperature (CT) versus SMAT at Room Temperature (RT)

SMAT-CT

- Fatigue resistance **+ 8%**
- Roughness **- 75%**
- Martensite depth **+ 50%**

SMAT-RT

- Surface hardening **+ 7%**
- Hardened depth **+ 30%**

Room Temperature